

Automatic Feynman diagram generation for nonlinear optical spectroscopies and application to fifth-order spectroscopy with pulse overlaps

Cite as: J. Chem. Phys. **154**, 034109 (2021); <https://doi.org/10.1063/5.0024105>

Submitted: 04 August 2020 . Accepted: 20 December 2020 . Published Online: 19 January 2021

 Peter A. Rose, and  Jacob J. Krich

COLLECTIONS

Paper published as part of the special topic on [Excitons: Energetics and Spatio-temporal Dynamics EXEN2020](#)



View Online



Export Citation



CrossMark

ARTICLES YOU MAY BE INTERESTED IN

[Efficient numerical method for predicting nonlinear optical spectroscopies of open systems](#)

The Journal of Chemical Physics **154**, 034108 (2021); <https://doi.org/10.1063/5.0024104>

[Relaxation dynamics through a conical intersection: Quantum and quantum-classical studies](#)

The Journal of Chemical Physics **154**, 034104 (2021); <https://doi.org/10.1063/5.0036726>

[Using quantum annealers to calculate ground state properties of molecules](#)

The Journal of Chemical Physics **154**, 034105 (2021); <https://doi.org/10.1063/5.0030397>



New

Your Qubits. Measured.

Meet the next generation of quantum analyzers

- Readout for up to 64 qubits
- Operation at up to 8.5 GHz, mixer-calibration-free
- Signal optimization with minimal latency

Find out more



Automatic Feynman diagram generation for nonlinear optical spectroscopies and application to fifth-order spectroscopy with pulse overlaps

Cite as: J. Chem. Phys. 154, 034109 (2021); doi: 10.1063/5.0024105

Submitted: 4 August 2020 • Accepted: 20 December 2020 •

Published Online: 19 January 2021



View Online



Export Citation



CrossMark

Peter A. Rose^{1,a)}  and Jacob J. Krich^{1,2} 

AFFILIATIONS

¹Department of Physics, University of Ottawa, Ottawa, Ontario K1N 6N5, Canada

²School of Electrical Engineering and Computer Science, University of Ottawa, Ottawa, Ontario K1N 6N5, Canada

Note: This paper is part of the JCP Special Topic on Excitons: Energetics and Spatio-Temporal Dynamics.

a) Author to whom correspondence should be addressed: prose036@uottawa.ca

ABSTRACT

Perturbative nonlinear optical spectroscopies are powerful methods to understand the dynamics of excitonic and other condensed phase systems. Feynman diagrams have long provided the essential tool to understand and interpret experimental spectra and to organize the calculation of spectra for model systems. When optical pulses are strictly time ordered, only a small number of diagrams contribute, but in many experiments, pulse-overlap effects are important for interpreting results. When pulses overlap, the number of contributing diagrams can increase rapidly, especially with higher order spectroscopies, and human error is especially likely when attempting to write down all the diagrams. We present an automated Diagram Generator (DG) that generates all the Feynman diagrams needed to calculate any n th-order spectroscopic signal. We characterize all perturbative nonlinear spectroscopies by their associated phase-discrimination condition as well as the time intervals where pulse amplitudes are nonzero. Although the DG can be used to automate impulsive calculations, its greatest strength lies in automating finite pulse calculations where pulse overlaps are important. We consider third-order transient absorption spectroscopy and fifth-order exciton–exciton interaction 2D (EEI2D) spectroscopy, which are described by six or seven diagrams in the impulsive limit, respectively, but 16 or 240 diagrams, respectively, when pulses overlap. The DG allows users to automatically include all relevant diagrams at a relatively low computational cost, since the extra diagrams are only generated for the inter-pulse delays where they are relevant. For EEI2D spectroscopy, we show the important effects of including the overlap diagrams.

Published under license by AIP Publishing. <https://doi.org/10.1063/5.0024105>

I. INTRODUCTION

Nonlinear optical spectroscopies (NLOSs) are powerful tools for elucidating excited state dynamics of a wide variety of condensed phase systems and have been particularly important for determining the evolution of excitonic systems.^{1–12} Interpretation of data-rich NLOS signals is centered on Feynman diagrams, which conveniently graphically summarize time-dependent perturbation theory contributions to the signals.¹³ These diagrams give a visual understanding of what types of excited- and ground-state dynamics and/or

coherences are probed and can be straightforwardly turned into calculations of contributions to signals. In many cases, diagrams can be determined to give zero contribution without a complicated calculation, making theoretical interpretation easier and calculation less expensive.

When pulse durations are shorter than system dynamics—the impulsive limit—the number of contributing diagrams is often small, especially for third-order spectroscopies. It has been easiest to build intuition about the experimental signatures of particular excitonic processes by considering the impulsive limit.^{2,3,5–7,14–21}

When pulse durations are similar to the timescale of system evolution, however, the effects of pulse overlaps—where the tail of a nominally earlier pulse arrives after the beginning of a nominally later pulse—become important to accurately model and understand experimental results.^{22–34} Considering such processes requires many more contributing diagrams. Higher-order spectroscopies, in both the impulsive and pulse-overlap limits, also involve rapidly increasing numbers of contributing diagrams. Human error and fatigue in determining these diagrams accurately become increasingly likely as their numbers proliferate.

We present here an automated Feynman Diagram Generator (DG), which allows convenient, fast, and accurate determination of the diagrams contributing to a particular spectroscopy. We describe all perturbative nonlinear spectroscopies by their associated phase-discrimination conditions. These conditions allow description of non-collinear phase-matching, collinear phase-cycling, and combinations of the two.^{13,16,21,35–40} Users input those conditions and the time intervals in which their pulses are nonzero, and the DG produces a list of contributing diagrams. This list can be passed directly to calculation engines to predict the associated spectroscopic signals or can be drawn in the standard diagrammatic format for review. The DG is part of a set of NLOS tools called the Ultrafast Spectroscopy Suite (UFSS), which also contains methods to generate Hamiltonians or Liouvillians for vibronic systems and to calculate the contributions from each diagram,^{41,42} but its output diagrams can be used with other computational tools or analytic methods to calculate spectroscopic signals.^{7,19,23,30,31,43–52} The DG is free and open-source software written in Python, available for download from GitHub.

The DG (also the larger UFSS) is designed to make simple the inclusion of the effects of finite-duration pulses in NLOS. While modeling often considers the impulsive limit, pulse-overlap effects can dominate third-order signals such as two-dimensional photon echo (2DPE) spectroscopy, even outside of what is commonly thought of as the pulse-overlap window.³³ 2DPE is usually calculated using six time-ordered diagrams (three for the rephasing and three for the non-rephasing pathway). When pulses overlap, up to 16 diagrams (shown in Fig. 1) contribute to the signal.⁵³ These 16 diagrams have been written down by hand and used for calculations in the past.

In higher-order methods, such as fifth-order exciton–exciton interaction 2D (EEI2D) spectroscopy, there are seven Feynman diagrams in the impulsive limit.²⁰ We show that outside the impulsive limit, EEI2D requires up to 240 Feynman diagrams. This number of diagrams is too large for generation by hand, and as a result, we do not believe that a calculation with all these diagrams has previously been attempted in the perturbative limit. References 12 and 54 consider finite pulse effects from time-ordered diagrams for several fifth-order spectroscopies. We use EEI2D as our key example of the application of automated diagram generation, showing that (1) these extra overlap diagrams can be generated and their contributions calculated with a surprisingly small extra computational cost and that (2) finite pulse effects arising from non-time-ordered diagrams can provide significant modifications to a sample EEI2D spectra, which can be important for the interpretation of experimental results.

The DG automatically creates all the diagrams that satisfy a given phase-discrimination condition. Since the DG is

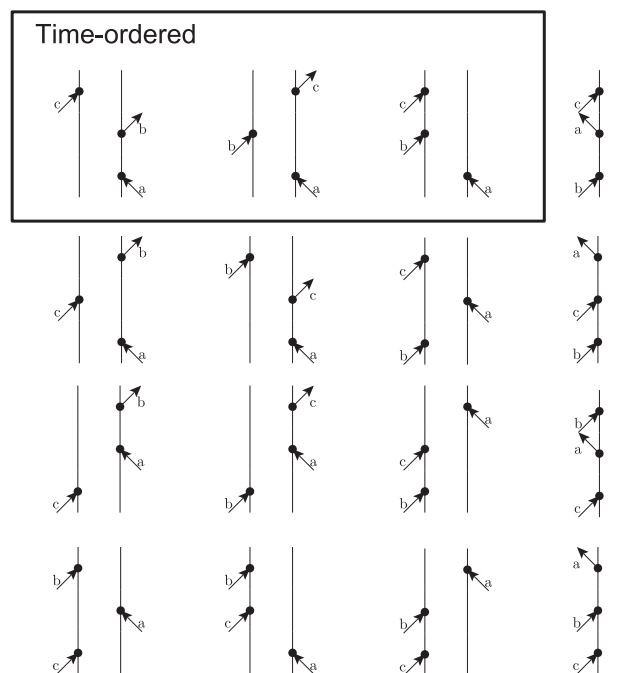


FIG. 1. All diagrams needed to calculate the rephasing 2DPE signal. The box encloses the three time-ordered diagrams that are typically calculated. The other diagrams contribute to the signal when two or more pulses overlap. These diagrams were automatically generated and drawn using the diagram generator (DG). The DG can produce both double-sided diagrams, as shown, and pairs of single-sided diagrams for equivalent wavefunction calculations.

computationally inexpensive compared to evaluating the contribution of each diagram, in UFSS, the DG is run for each set of the desired pulse delays. It determines whether pulses overlap, and thus whether overlap diagrams contribute, allowing computation of only causal diagrams for each set of pulse delays. This determination provides significant computational time savings, since the large number of overlap diagrams only need to be calculated at the (usually small) proportion of pulse delays where they contribute. We further show that heavy-tailed pulse envelopes, such as Lorentzians, require calculation of overlap diagrams out to longer delay times than Gaussian pulse envelopes.

We begin with an overview of perturbative spectroscopy calculations in Sec. II in order to establish the construction of Feynman diagrams, with a unified perspective on both phase matching and phase cycling spectroscopies. We describe the algorithm of the DG in Sec. III, including optional methods to reduce the number of diagrams, depending on the system and spectroscopy considered. We demonstrate the utility of the DG by exploring EEI2D spectroscopy in Sec. IV. We consider the same model system as in Ref. 55 and show that when optical pulses have slightly longer durations than those considered in that work, neither the impulsive limit nor the time-ordered diagrams with pulse-shape effects included accurately predict spectra. The calculation with all 240 diagrams requires less than twice the time as that required for the calculation using only the seven time-ordered diagrams, despite considering 34 times as

many diagrams. These results underscore the importance of including all the additional 233 overlap diagrams, as well as the utility of the DG in not only generating these diagrams but also automatically determining the conditions in which they contribute.

II. NONLINEAR SPECTROSCOPY AND FEYNMAN DIAGRAMS

We begin by establishing the standard perturbative framework of nonlinear optical spectroscopy, from which Feynman diagrams are defined.¹³ Consider a system with density matrix ρ , which evolves in the absence of perturbation according to

$$\rho(t) = \mathcal{T}_0(t, t')\rho(t'),$$

where \mathcal{T}_0 is a time evolution operator. We restrict the following discussion to the case of Hamiltonian systems or Markovian open systems in which $\mathcal{T}_0(t, t') = \mathcal{T}_0(t - t')$, which must be known or approximated in order to complete calculations, but the resulting diagrams are broadly applicable to non-Markovian situations as well. For the purposes of diagram generation, however, we simply need to assume that \mathcal{T}_0 exists. We also define the differential time evolution operator \mathcal{L}_0 , so

$$\frac{d\rho(t)}{dt} = \mathcal{L}_0\rho(t).$$

The perturbative optical fields are described as classical electric fields $\mathbf{E}(t)$, which interact with the system in the electric-dipole approximation through the perturbation Hamiltonian

$$H'(t) = -\boldsymbol{\mu} \cdot \mathbf{E}(t), \quad (1)$$

where $\boldsymbol{\mu}$ is the electric dipole operator. Then, the time evolution of the system is

$$\frac{d\rho(t)}{dt} = \mathcal{L}_0\rho(t) - \frac{i}{\hbar}[H'(t), \rho(t)]. \quad (2)$$

This form is the basis for diagrammatic perturbation theory in $\mathbf{E}(t)$.

We describe $\mathbf{E}(t)$ as a sum over L pulses, where each pulse is denoted by a lowercase letter starting from a . A typical third-order signal is calculated using up to four pulses. We write the electric field as

$$\mathbf{E}(t) = \sum_{j=a,b,\dots,L} \mathbf{e}_j \varepsilon_j(t) + \mathbf{e}_j^* \varepsilon_j^*(t), \quad (3)$$

where \mathbf{e}_j is the possibly complex polarization vector and the amplitude ε_j of each pulse is defined with envelope A_j , central frequency ω_j , wavevector \mathbf{k}_j , and phase ϕ_j as

$$\varepsilon_j(t) = A_j(t - t_j)e^{-i(\omega_j(t-t_j) - \mathbf{k}_j \cdot \mathbf{r} - \phi_j)},$$

where t_j is the arrival time of each pulse. We make the physical assumption that each pulse is zero outside the finite interval $[t_{j,\min},$

$t_{j,\max}]$. The DG uses this range to determine when pulses overlap; the form of $A_j(t)$ is unimportant for diagram generation. The light-matter interaction is a sum over the rotating (ε_j) and counter-rotating (ε_j^*) terms. In the rotating wave approximation (RWA), the rotating terms excite the ket-side and de-excite the bra-side of the density matrix, respectively, and the counter-rotating terms excite the bra-side and de-excite the ket side, respectively.¹³

We treat the effect of the optical fields using standard time-dependent perturbation theory and assume that at time t_0 , the system is in a stationary state of \mathcal{L}_0 , which is $\rho^{(0)}$. Then,

$$\rho(t) = \rho^{(0)} + \rho^{(1)}(t) + \rho^{(2)}(t) + \dots, \quad (4)$$

where¹³

$$\rho^{(n+1)}(t) = \int_0^\infty dt' \mathcal{T}_0(t') \left[\frac{-i}{\hbar} \boldsymbol{\mu} \cdot \mathbf{E}(t - t'), \rho^{(n)}(t - t') \right]. \quad (5)$$

Using Eq. (3), we define $\rho^{(n+1)}(t)$ as a sum over four types of terms,

$$\rho^{(n+1)}(t) = \sum_j (K_j + K_{j^*} + B_j + B_{j^*}) \rho^{(n)}(t), \quad (6)$$

where K_j and B_j are superoperators representing ket- and bra-side actions, respectively, of the rotating terms of pulse j on ρ , while K_{j^*} and B_{j^*} give the equivalent counter-rotating terms. By inspection of Eq. (5), all four types of terms in Eq. (6) can be compactly defined as

$$O_{j^{(*)}} = \eta_O \frac{i}{\hbar} \int_0^\infty dt' \mathcal{T}_0(t') (\boldsymbol{\mu}^O \cdot \mathbf{e}_j^{(*)} \varepsilon_j^{(*)}(t - t')), \quad (7)$$

where $O = K, B$, $\eta_K = 1$, and $\eta_B = -1$, and we define dipole superoperators $\boldsymbol{\mu}^K \rho \equiv \boldsymbol{\mu} \rho$ and $\boldsymbol{\mu}^B \rho \equiv \rho \boldsymbol{\mu}$. The operators $\{O_{j^{(*)}}\}$ are the building blocks for all perturbative spectroscopies. The full $\rho^{(n)}$ is constructed from the unperturbed state $\rho^{(0)}$ as

$$\rho^{(n)}(t) = \left[\sum_{j=a,b,\dots,L} (K_j + K_{j^*} + B_j + B_{j^*}) \right]^n \rho^{(0)}, \quad (8)$$

which involves $(4L)^n$ terms when the exponent and sum are fully expanded. Each of these terms is a sequence of n applications of $O_{j^{(*)}}$ and can be represented by a Feynman diagram. Most of these diagrams are unimportant for any given spectroscopy, and the subset of diagrams that contributes to a particular experiment is determined by the set of optical pulses and a phase-discrimination condition.

Regardless of the computational details used to calculate the $\{O_{j^{(*)}}\}$, all perturbative calculations can be represented and organized using the same Feynman diagrams, and thus, the DG is useful for any perturbative spectroscopy algorithm. For example, the UFSS contains two methods for calculating the action of the $O_{j^{(*)}}$ operators, which are derived for closed systems in Ref. 41 and for open systems in Ref. 42. The integral form of the $\{O_{j^{(*)}}\}$ in Eq. (7) is convenient for UF² and is the open-system analog of similar expressions derived for wavefunctions.^{43,48}

The two most widely used phase-discrimination conditions are phase matching and phase cycling. Phase-matching conditions are achieved by using pulses that travel along different directions denoted by wavevectors \mathbf{k}_j , converging to interact with a sample that is assumed to be uniform over a volume large compared to the wavelength of the pulses.¹³ The pulses induce a polarization field in the sample $\mathbf{P}(t) = \langle \mu \rho(t) \rangle$, which produces radiation in all directions. A detector placed in a direction that satisfies the phase-matching condition $\mathbf{k}_d = \sum_j m_j \mathbf{k}_j$, where m_j are integers, is sensitive to a polarization field that is described by only a subset of diagrams. Often one is interested in the lowest-order signal in perturbation theory that contributes to the given phase-discrimination condition. Heterodyne detection with a local oscillator (LO) allows full determination of the amplitude and phase of the emitted radiation.

For example, 2D photon echo (2DPE) signals involve three pulses, a , b , and c , that interact with the sample and a fourth LO pulse d . The 2DPE rephasing and non-rephasing signals are measured with detectors placed in the $\mathbf{k}_d = -\mathbf{k}_a + \mathbf{k}_b + \mathbf{k}_c$ (see Fig. 1) and $\mathbf{k}_d = \mathbf{k}_a - \mathbf{k}_b + \mathbf{k}_c$ directions, respectively. These signals are calculated using

$$\begin{aligned} \mathbf{P}_{\mathbf{k}_d}^{(3)}(t) &= \langle \mu \rho_{\mathbf{k}_d}^{(3)}(t) \rangle \\ \tilde{\mathbf{P}}_{\mathbf{k}_d}^{(3)}(\omega) &= \int_{-\infty}^{\infty} dt e^{i\omega t} \mathbf{P}_{\mathbf{k}_d}^{(3)}(t) \\ S_{\mathbf{k}_d}^{(3)}(\omega) &= \text{Im} \left[\tilde{\epsilon}_d^*(\omega) \mathbf{e}_d \cdot \tilde{\mathbf{P}}_{\mathbf{k}_d}^{(3)}(\omega) \right], \end{aligned}$$

where $S_{\mathbf{k}_d}^{(3)}(\omega)$ are the signals and $\rho_{\mathbf{k}_d}^{(3)}(t)$ is the portion of $\rho^{(3)}(t)$ that produces radiation in the \mathbf{k}_d direction; the primary purpose of diagrammatic perturbation theory is to organize the efficient calculation of $\rho_{\mathbf{k}_d}^{(3)}(t)$ without needing to calculate all contributions to $\rho^{(3)}(t)$.

An alternative phase discrimination method uses phase cycling over the relative phases of collinear pulses. This method generally detects a signal proportional to an excited state population, such as fluorescence or photocurrent.^{16,35,38,39} A fourth-order signal $S_d^{(4)}(t)$ in such a setup is calculated as

$$S_d^{(4)}(t) = \left\langle Q \rho_d^{(4)}(t) \right\rangle,$$

where Q is a projection operator onto the relevant excited electronic states and $\rho_d^{(4)}(t)$ includes only those contributions to $\rho^{(4)}(t)$ that contribute to the chosen phase-cycling condition. Combinations of phase-matching and phase-cycling are also possible and just as easily described in the DG.³⁶

For example, the 2DPE rephasing signal is composed of the 16 diagrams in Fig. 1, which were automatically generated and drawn using the DG. If, however, $t_{b,\min} > t_{a,\max}$ and $t_{c,\min} > t_{b,\max}$ (that is, the pulses are time ordered), then only three diagrams contribute, as shown in the black box.

The operators $\{O_{j^{(*)}}\}$ as an abstract concept have previously been introduced in various forms.^{43,48} To our knowledge, they have not been used for the purposes of automated calculations before. In Sec. III, we describe how users input the pulse intervals and phase discrimination conditions and present the algorithm that produces the relevant diagrams. In Sec. IV, we demonstrate the DG by

using up to 240 diagrams and show the importance of including the full set of diagrams when performing simulations with finite pulse durations.

III. DIAGRAM GENERATOR

The user of the DG inputs the desired phase discrimination condition and pulse intervals, and the DG automatically generates all Feynman diagrams. The DG is much less computationally expensive than the evaluation of the contribution from each diagram, so it is intended to be rerun for each set of the desired pulse delays. The DG then returns pulse-overlap diagrams only when the pulse overlaps allow them to contribute. This package generates diagrams as a list of the operators $\{O_{j^{(*)}}\}$ defined in Eq. (7). The Ultrafast Ultrafast (UF²) and Runge–Kutta–Euler (RKE) tools outlined in Ref. 42 and included in UFSS are designed to interpret this list and produce spectra. Alternatively, the generated diagrams can be exported to another calculation engine. The DG can also draw them for inspection.

Feynman diagrams are determined by the number of pulses and the phase-discrimination condition. Phase-discrimination determines the number of interactions with the rotating or counter-rotating part of each pulse that contributes to the measured signal. The user inputs the number of each type of interaction as a list of tuples, $[(n_r^a, n_c^a), (n_r^b, n_c^b), \dots, (n_r^L, n_c^L)]$. This list corresponds to detection with $\mathbf{k}_d = \sum_{j=a,b,\dots,L} (n_r^j - n_c^j) \mathbf{k}_j$ in the case of phase matching and to detection of signals in phase with $\sum_{j=a,b,\dots,L} (n_r^j - n_c^j) \phi_j$, where ϕ_j are the modulated phases, in the case of phase cycling.³⁵ The order of spectroscopy is given by $n_{\text{total}} = \sum_{j=a,b,\dots,L} n_r^j + n_c^j$. In order to determine which diagrams are causally allowed, the user must also input the time intervals $[t_{j,\min}, t_{j,\max}]$ when each pulse is nonzero as a list. The user updates this list for each set of pulse delay times desired. The number of diagrams that must be considered when dealing with finite pulses expands dramatically as one considers higher-order signals, such as exciton–exciton interaction 2D spectra (the three-pulse fifth-order signal measured in the $\mathbf{k}_d = -2\mathbf{k}_1 + 2\mathbf{k}_2 + \mathbf{k}_3$ direction; see Sec. IV), where the number of time-ordered diagrams is 7.⁵⁵ However, when all pulses overlap, there are 240 diagrams.

We outline the steps for determining all diagrams that contribute to the signal for a given pulse configuration in Fig. 2, which includes the general scheme and two examples.

- (1) Starting from $[(n_r^i, n_c^i)]_{i=a,b,\dots,L}$, we begin with a canonical list of interactions, where we list the pulses in the order of the pulse number starting from a , with rotating terms coming before counter-rotating terms (see Fig. 2 for examples). The length of the resulting list is n_{total} . For each pulse, there are n_r^j repetitions of “ j ” with the rotating term and n_c^j repetitions of “ j^* ” with the counter-rotating term, as shown in Fig. 2. We then generate all unique permutations of this canonical list of interactions. The number of unique permutations is

$$\frac{n_{\text{total}}!}{\prod_i n_r^i! n_c^i!}.$$

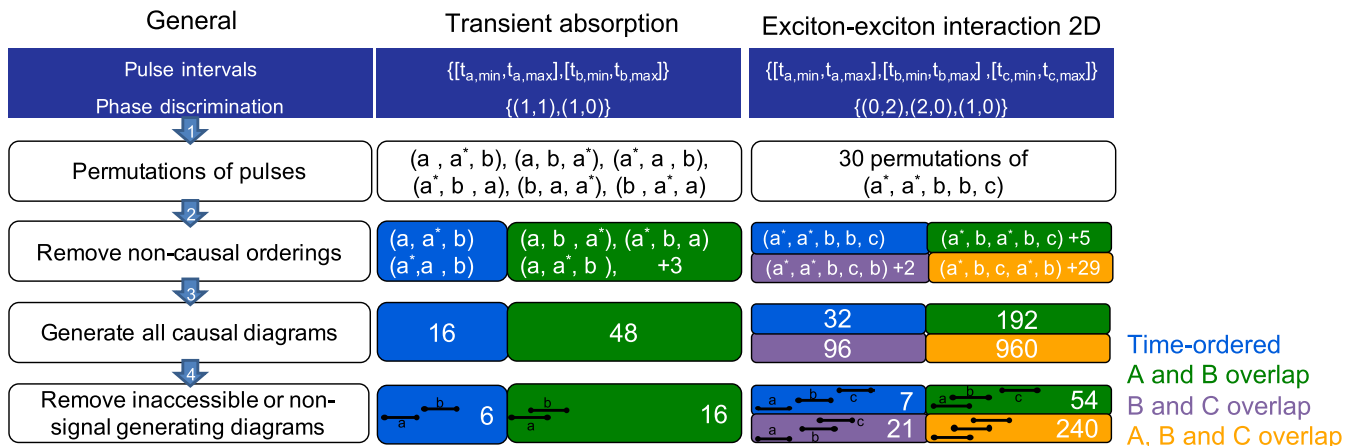


FIG. 2. Graphical outline of automated diagram generation. Left column is the general case, while the center and right columns show specific examples. User inputs of pulse intervals and phase discrimination of the desired experiment are in the top box. The steps of the algorithm, numbered in the arrows, are described in the main text. After step 3, the numbers in the boxes indicate the number of diagrams at that stage. Blue boxes show results with non-overlapping pulses. Green ones show results with pulses a and b overlapping, purple ones show results with pulses b and c overlapping, and gold ones show results with pulses a , b , and c all overlapping. Black bars in the bottom row graphically indicate these pulse overlaps.

- Using the list of pulse intervals $\{[t_{j,\min}, t_{j,\max}]\}_{j=a,b,\dots,L}$, non-causal orderings are removed. For each permutation of the time-ordered list, we check whether t_{\min} of each pulse occurs before t_{\max} of each following pulse in the list and remove the permutation if not.
- For each permutation from step 2, we generate all the allowed diagrams that satisfy the phase-discrimination conditions. Each interaction can occur on either the ket-side ($K_{j(*)}$) or the bra-side ($B_{j(*)}$), giving $2^{n_{\text{total}}}$ diagrams associated with each permutation from step 2. For example, the interaction a^* can act as K_{a^*} or as B_{a^*} , while the interaction b can act as either K_b or B_b .

At this point, we have the maximum number of diagrams that could contribute to the calculation, given the phase-discrimination condition and pulse intervals. However, many of these diagrams do not contribute under common assumptions. Using some minimal information about the material system that is being modeled, many of these diagrams can be removed in the optional step 4.

- (Optional)
 - Keep only diagrams that remain in accessible states. For instance, consider optical spectroscopy of a system that has three optically separated manifolds, each separated by an energy gap E_g . If the temperature is much less than E_g , we can approximate that the initial thermal state is entirely in the ground-state manifold. Any diagram that includes excitation above the highest manifold or de-excitation from the lowest manifold is removed. We track the number of optical excitations by assigning manifold indices for both the ket and bra sides of a density matrix. We say that the initial density matrix $\rho^{(0)}$ is entirely composed of ground-state populations, and therefore, it has manifold indices $[0, 0]$. We then assign the following rules describing the action of the $O_{j(*)}$ operators:

$$K_j : [+1, 0],$$

$$K_{j^*} : [-1, 0],$$

$$B_j : [0, -1],$$

$$B_{j^*} : [0, +1].$$

We apply these rules in succession for a diagram and track the indices $[i, l]$ after each interaction. If either i or l drop below 0 or rise above the maximum allowed manifold, the diagram is removed. When the manifolds are coupled by relaxation processes, we no longer remove diagrams that rise above the allowed maximum manifold, since population can decay to a lower manifold and then be excited up again by a subsequent interaction. We do still remove diagrams where i or l drop below zero.

- The integer logic of part 4(a) is also helpful in determining which diagrams contribute to the final signal. For spectroscopies that measure the emitted polarization field, we are interested in the object $\text{Tr}[\mu\rho]$. Typically in optical spectroscopy, μ connects only adjacent manifolds (either because this is an accurate model for the dipole operator or because the measurement bandwidth only supports one-manifold transitions). The components of ρ that contribute are then coherences between adjacent optical manifolds. Therefore, we filter out all diagrams except those that end in a state $[i + 1, i]$ (note that the diagrams that end in $[i, i + 1]$ are physically valid; however, we do not calculate them, as they are the Hermitian conjugate pairs of the calculated diagrams¹³). Note that we again cannot apply this filter when \mathcal{T} includes inter-manifold relaxation.
- If the final observable is instead linked to excited-state populations, as in the case of fluorescence or photo-current detection, we look only for diagrams that end in

a population $[i, i]$, where $i > 0$. Again, we cannot apply this filter when \mathcal{T} includes inter-manifold relaxation.

Each of the diagram reductions from step 4 can be turned off with a flag or modified to suit an accurate model for the system in question. For example, in vibrational spectroscopy, rule 4(a) does not apply, but rules 4(b) or 4(c) (or modifications of them) may still apply. We include a variety of examples of step (4) in the Jupyter notebook `DiagramGeneratorExample.ipynb`, including an example of infrared vibrational transient absorption that cannot remove any of the causal diagrams and must use all 16 (48 for overlapping pulses) diagrams that come from step (3).

Thus far, we have described how the DG creates the double-sided Feynman diagrams associated with density-matrix-based calculations. The DG can also create the one-sided Feynman diagrams used for wavefunction-based calculations.^{13,48} This procedure begins by creating all relevant double-sided diagrams. Each double-sided diagram is converted to a pair of one-sided diagrams associated with the bra and ket wavefunctions. Since wavefunction-based calculations do not impose time-ordering between the bra and ket sides,¹³ several of the double-sided diagrams map onto the same pair of single-sided diagrams. After creating all the pairs of single-sided diagrams, we eliminate duplicates to avoid over-counting some pathways.

The DG both produces a full set of contributing diagrams to be calculated and updates that list as the pulse timings change. In the example three-pulse fifth-order spectroscopy considered in Sec. IV, the pulse delays vary to produce frequency-domain signals. Only a small number of pulse configurations have all three pulses overlapping. In those cases, 240 diagrams must be calculated, but as the pulse delays change, calculations can be reduced to 54, 21, or seven diagrams, all occurring automatically. Including overlap diagrams increases the number of required diagrams by a factor of over 30, but since diagrams are only included when pulse delays are required, calculations of frequency-domain spectra are only 1.5–5 times longer than those including only the seven time-ordered diagrams, depending upon which pulse delays are calculated.

IV. IMPORTANCE OF OVERLAP DIAGRAMS

Spectra are often calculated assuming impulsive pulses. Even when finite pulse shapes are considered, the overlap diagrams are often neglected, as in the only two studies of finite pulses in fifth-order spectroscopies of which we are aware.^{12,54} In some cases, these approximations are warranted, but sometimes, the overlap diagrams are important to understand signals both quantitatively and qualitatively. Here, we demonstrate an example where neglecting overlap diagrams leads to significant artifacts in the predicted spectra.

We consider a model system used in Ref. 55 to study exciton–exciton annihilation by three-pulse exciton–exciton interaction 2D (EEI2D) spectroscopy. The model consists of a dimer of two coupled three-level systems (3LS). The Hamiltonian takes the form

$$\begin{aligned}
 H_0 = & E_{gg}(|gg\rangle\langle gg|) + E_{eg}(|eg\rangle\langle eg| + |ge\rangle\langle ge|) \\
 & + J(|eg\rangle\langle ge| + h.c.) + E_{ee}(|ee\rangle\langle ee|) \\
 & + E_{fg}(|fg\rangle\langle fg| + |gf\rangle\langle gf|) + K(|fg\rangle\langle ee| + |gf\rangle\langle ee| + h.c.) \\
 & + E_{ef}(|fe\rangle\langle fe| + |ef\rangle\langle ef|) + L(|fe\rangle\langle ef| + h.c.) \\
 & + E_{ff}(|ff\rangle\langle ff|),
 \end{aligned}$$

where $E_{ij} = E_i + E_j$, with all the constants defined in Table I, $|g\rangle$, $|e\rangle$, and $|f\rangle$ are the ground, singly excited, and doubly excited states, respectively, of each 3LS, and $|uv\rangle = |u\rangle_1 \otimes |v\rangle_2$. Following Ref. 55, we consider relaxation processes at zero temperature for each isolated monomer unit from $|f\rangle_i$ to $|e\rangle_i$ at rate k_M and neglect relaxation from $|e\rangle_i$ to $|g\rangle_i$, since it is not important for exciton–exciton interactions. Reference 55 included relaxation using the stochastic Schrödinger equation, while we include relaxation using the Lindblad formalism with

$$\dot{\rho} = -\frac{i}{\hbar}[H_0, \rho] - \sum_{n \neq m} k_{nm} L[|m\rangle\langle n|]\rho,$$

where $|m\rangle$ and $|n\rangle$ are eigenstates of H_0 and the Lindblad superoperator $L[O]$ is defined by

$$L[O]\rho = O\rho O^\dagger - \frac{1}{2}O^\dagger O\rho - \frac{1}{2}\rho O^\dagger O.$$

We follow Ref. 55 by projecting the monomer relaxation rates into the eigenstates $|n\rangle$ with energy E_n . New relaxation rates coupling the eigenstates of H_0 are defined as

$$\begin{aligned}
 k_{nm} = & (|\langle n|fg\rangle|^2|\langle eg|m\rangle|^2 + |\langle n|gf\rangle|^2|\langle ge|m\rangle|^2 \\
 & + |\langle n|fe\rangle|^2|\langle ee|m\rangle|^2 + |\langle n|ef\rangle|^2|\langle ee|m\rangle|^2)k_M.
 \end{aligned}$$

The resulting rates range from 0.0075 fs⁻¹ to 0.0016 fs⁻¹ where the smallest rate corresponds to decay from the lowest-energy double-exciton state to the lowest-energy single-exciton state.

EEI2D is designed to probe the dynamics of the doubly excited states. Diagonalizing H_0 shows that the two optically bright doubly excited states are separated by 0.35 eV, corresponding to an oscillation period of $T_o = 12$ fs, which is the fastest important oscillation in this system. One generally assumes that pulses significantly shorter than this period will be well-approximated by impulsive pulses but that pulses that interact with the system on a comparable timescale

TABLE I. Values used in the Hamiltonian H_0 and bath coupling rates for the model dimer system studied using EEI2D (adapted from Ref. 55).

	E_g	E_e	E_f
Energy (eV)	0.0	1.0	2.2
	J	K	L
Coupling (eV)	0.2	0.1	0.05
	k_M		
Rate (fs ⁻¹)	0.015		

require more careful treatment. In this section, we study the effects of using Gaussian pulses with a full-width half-maximum (FWHM) of 15 fs, with a comparison to Lorentzian pulses at the end.

The perturbative calculations of optical signals were performed using the UF² method detailed in Ref. 42. UF² calculates the fifth-order polarization signal as a function of the delay time τ between pulses a and b and the delay time T between pulses b and c as

$$\mathbf{P}_{k_d}^{(5)}(\tau, T, t) = i\langle \mu \rho_{k_d}^{(5)}(t) \rangle,$$

where t is the time measured after the arrival of pulse c . The 2D frequency–frequency correlation spectrum is calculated as

$$\tilde{\mathbf{P}}_{k_d}^{(5)}(\omega_\tau, T, \omega_t) = \frac{1}{2\pi} \int_{-\infty}^{\infty} d\tau e^{-i\omega_\tau \tau} \int_{-\infty}^{\infty} dt e^{i\omega_t t} \mathbf{P}_{k_d}^{(5)}(\tau, T, t),$$

which is approximated using the discrete Fourier transform. We use $\tilde{\mathbf{P}}_{k_d}^{(5)}(\omega_\tau, T, \omega_t)$ as a proxy for the signal field, which would, in practice, be detected through heterodyne detection with a local oscillator.

We compare calculations of EEI2D spectra using three approximations: impulsive pulses, finite pulses with only time-ordered diagrams, and finite pulses including all diagrams. Figure 3(a) shows

the impulsive limit with a delay time of $T = 60$ fs. In keeping with Ref. 55, we perform all calculations with τ and t each ranging from 0 to 823 fs and multiply the τ and t axes with a Gaussian window function of $\sigma = 200$ fs to avoid ringing effects from the discrete Fourier transform. We calculate spectra for 275 values of τ and t , which are more than sufficient to produce well-resolved frequency–frequency spectra. Reference 55 performs calculations in the impulsive limit and states that calculations using time-ordered diagrams with 5 fs FWHM pulses are visually nearly identical to the impulsive limit, which we also find. Finite pulse effects are, unsurprisingly, unimportant when the pulse durations are shorter than T_0 , the fastest timescale in the system. We use this model system to illustrate the differences that occur with only modestly longer pulses.

We consider Gaussian pulses with FWHM of 15 fs, similar to T_0 . Figure 3(b) shows calculations using finite pulses but only the seven time-ordered diagrams, showing clear differences from the impulsive limit in 3(a). Figure 3(c) shows results using the same finite pulses but including all the 233 additional pulse overlap diagrams at delay times when they are required. The visual difference between Figs. 3(b) and 3(c) demonstrates the importance of including pulse-overlap diagrams in addition to finite pulse effects in time-ordered diagrams. Simply adding finite pulse effects to the time-ordered diagrams is not sufficient for making good spectroscopic predictions.

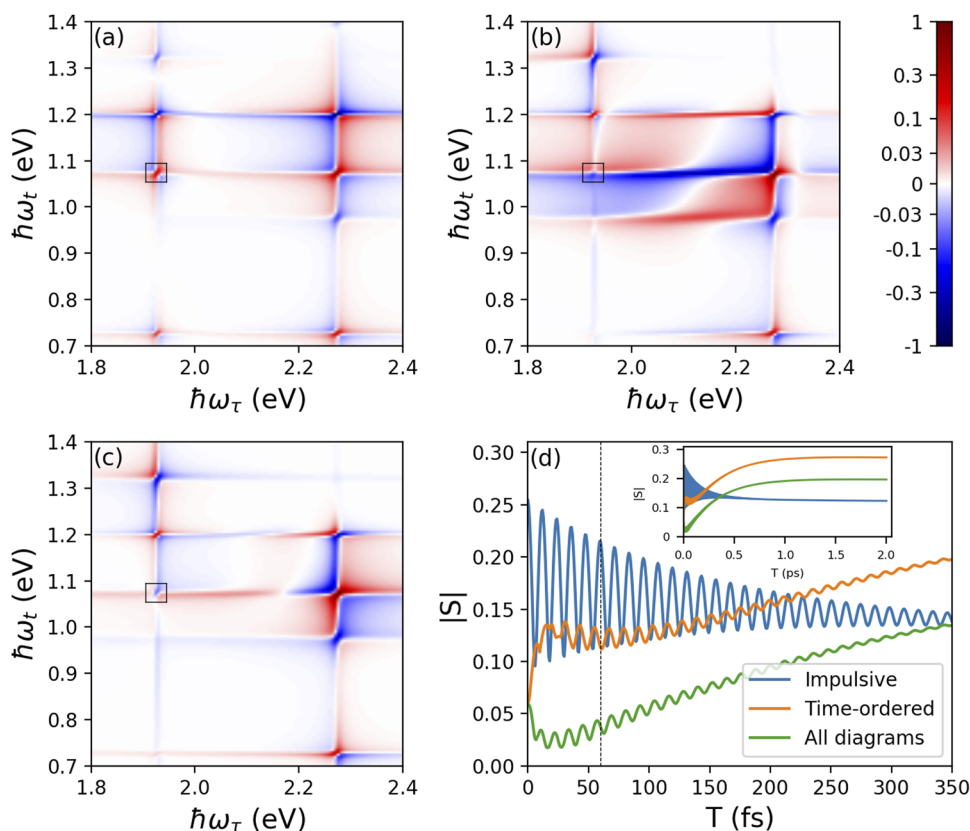


FIG. 3. (a)–(c) Real part of the EEI2D spectrum at a delay time of $T = 60$ fs for a dimer of three-level systems with a relaxation rate of 0.015 fs^{-1} , as described in the text, with different electric field shapes. Horizontal axes show the Fourier transform of the delay time τ between the first and second pulses. Vertical axes show the detection frequency. EEI2D spectra were calculated for 275×275 values of τ , t and then Fourier transformed. Note the signed-logarithmic color scale. (a) Impulsive calculation, which requires only time-ordered diagrams, (b) 15 fs FWHM Gaussian pulses using only time-ordered diagrams, and (c) 15 fs FWHM Gaussian pulses including all 54 diagrams that contribute to this T . (a)–(c) are normalized independently so that the largest peak has a magnitude of 1. (d) Maximum of the absolute value of the signal contained within the black boxes in (a)–(c) as a function of delay time T . Dashed line shows T used in (a)–(c). The inset shows a longer time window and the steady state that is reached by 1 ps. The impulsive and time-ordered calculations both quantitatively and qualitatively deviate from the full calculation.

Figure 3(d) shows the magnitude of the cross peak contained in the solid box in panels (a)–(c), and the oscillation period T_o is clearly visible. The oscillations at that peak correspond to absorption into one and emission from another doubly excited eigenstate of H_0 . This peak is clearly visible in the impulsive limit in Fig. 3(a) but is dominated by significant horizontal streaks in Fig. 3(b), which bleed over from the stronger peak at $\hbar\omega_\tau = 2.3$ eV. This significant extension of the peaks in the ω_τ direction is an artifact of neglecting the overlap diagrams, demonstrated by its removal in Fig. 3(c). Figure 3(d) shows that both the visibility of the oscillation and the overall evolution of the envelope are qualitatively different in the three studied approximations. We vary T from 0 ps to 2 ps for a total of 2667 different values of T . At long T (shown in the inset), the doubly excited states decay and there is a static excited state absorption signal from the singly excited population, with the timescale of saturation and oscillation decay matching the slowest k_{nm} . Neither impulsive nor time-ordered calculations with finite pulses accurately predict this EEI2D spectrum despite using an ultrafast optical pulse.

Note that the differences between the full calculation and the one using only the time-ordered diagrams persist even with delay times T much greater than the pulse durations. In constructing $\tilde{\mathbf{P}}_{k_d}^{(5)}(\omega_\tau, T, \omega_t)$, contributions with τ, t smaller than the pulse duration are always included, making pulse-overlap effects apparent even at long T and requiring calculation of the overlap diagrams. Since the DG only produces the extra diagrams for time delays that merit their evaluation, the full calculation is not much more expensive than the case with seven time-ordered diagrams. For example, the calculation of the green and orange curves in Fig. 3(d), out to 350 fs, took 33 min and 17 min on a 2017 MacBook Pro, respectively, and included over 120 000 combinations of τ and T . The equivalent curves out to 2 ps, as in the inset, required 155 min

and 93 min with the same density of T points; those involved over 700 000 pulse delay combinations. Even though the full calculation includes contributions from 34 times more diagrams, it required less than twice the time to run than the time-ordered calculation.

The DG determines which diagrams contribute based solely upon the user-chosen intervals where the pulses are nonzero. For well-behaved pulses such as Gaussians with standard deviation σ , convergence of spectra within 1% is obtained for the results in Fig. 3 when the pulses are declared to be zero after 4σ . However, for pulses with heavy tails, extra care must be taken to determine the correct pulse interval. We compare Gaussian pulses, as used in Fig. 3, to Lorentzian pulses, which have heavy tails. Figure 4 shows the weight $D \int d\omega_t |\tilde{\mathbf{P}}_d^{(5)}(\tau, T, \omega_t)|$ for each of the 240 diagrams d as a function of τ at $T = 100$ fs for the system in Fig. 3, where $\tilde{\mathbf{P}}_d^{(5)}$ is the signal due to a single diagram and D is chosen so that at $\tau = 0$, the largest weight of a time-ordered diagram is 1. We consider Gaussian and Lorentzian pulse envelopes with the same FWHM of 15 fs.

We observe that for both sets of pulses, at $\tau = 0$, all 47 a, b overlap diagrams (green) have similar weight and therefore must be calculated, and the same is true for all 233 overlap diagrams at $\tau = T = 0$ (not shown). With Gaussian pulses, all the overlap diagrams decay rapidly when τ exceeds the nominal pulse duration and are negligible when $\tau > 30$ fs. In contrast, with Lorentzian pulses of the same nominal duration, even some diagrams where pulse c arrives before pulse a or b (shown in gold) are surprisingly close in weight to the time-ordered diagrams at $\tau = 0$, even though the center of pulse c arrives 100 fs after the first two. Furthermore, some of the a, b overlap diagrams (green) continue to have weight equal to time-ordered diagrams (blue) for τ approaching 60 fs, four times the pulse FWHM; given the large number of overlap diagrams, their contributions must be calculated even for considerably larger τ . It is clear that

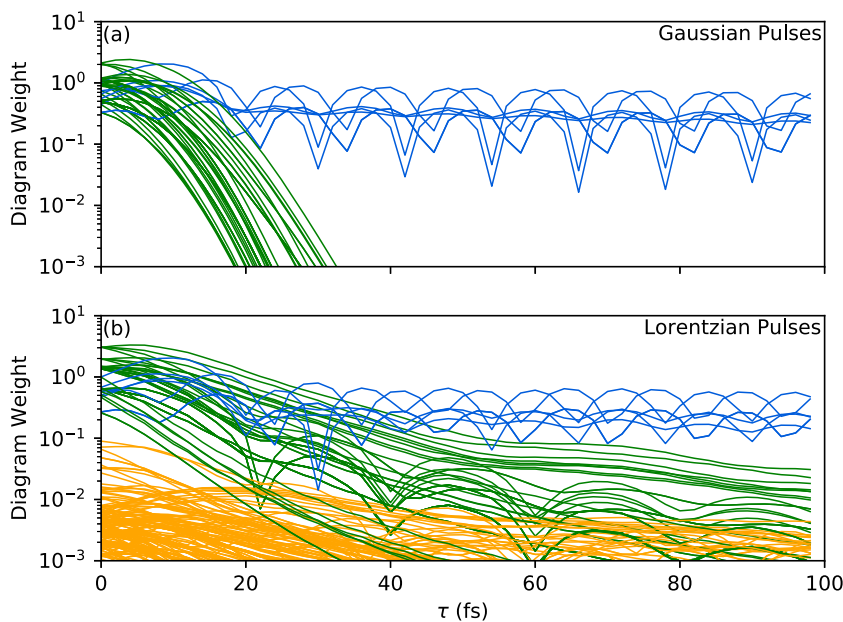


FIG. 4. Weight of all 240 EEI2D diagrams for the same system as in Fig. 3 at $T = 100$ fs as a function of τ for 15 fs FWHM pulses with (a) Gaussian and (b) Lorentzian time-domain envelopes. Blue lines show the weight of the seven time-ordered diagrams. Green lines show the weight of the 47 additional diagrams that contribute when pulses a and b overlap. Panel (b) also shows the weights of 176 diagrams that contribute only when all three pulses overlap (gold), whose weights are too small to appear in (a); 10 more orange lines have weights less than 10^{-3} . Diagram weights are normalized so that the strongest time-ordered diagram has a weight of 1 at $\tau = 0$. Line colors for each set of diagrams match those in Fig. 2.

in the case of Lorentzian or other heavy-tailed pulse envelopes, care must be taken in choosing the pulse intervals for use with the DG, and users are encouraged to ensure that their results are converged. Choosing a large pulse interval ensures accuracy but increases the computational cost as more overlap diagram contributions must be calculated.

Many ultrashort optical pulses have heavy tails in the time domain, and Ref. 33 showed experimental evidence that pulse overlap effects can extend for up to 100 fs when using 17 fs FWHM pulses in 2DPE experiments. They attributed this effect to the significant wings on the pulse envelopes, which is consistent with our analysis of Lorentzian pulses.

V. CONCLUSION

We have presented the diagram generator (DG), a tool for automatically generating the Feynman diagrams that contribute to perturbative nonlinear optical spectroscopies. The DG automatically determines when pulses overlap and only generates extra overlap diagrams when required. This automated process allows users to get the full advantage of including all causally allowed diagrams with a low computational cost.

We have shown that including these overlap diagrams can be important in correctly predicting or interpreting spectra when pulses are not in the impulsive limit. Using EEI2D as an example, we have shown significant errors when using only the time-ordered diagrams with pulses whose duration are similar to the dynamics of the system. We have also shown that overlap diagrams can make significant contributions to the signal for delay times that are large relative to the pulse durations, when those pulses have heavy temporal tails, as in the case of Lorentzian pulses.

The DG is one module of the larger ultrafast spectroscopy suite. The other components in UFSS are described in Refs. 41 and 42. Taken together, the UFSS is a tool for automatically calculating arbitrary-order spectroscopic signals while accounting for the effects of finite pulse shapes, which can be of arbitrary form. The diagrams produced by the DG can also be used in other analytical or numerical tools. The DG can be used for determining all the diagrams that contribute to any order spectra, whether in the impulsive limit or with finite pulses. The DG may open the door to more easily calculating higher-order corrections to commonly used third-order spectroscopies and may lend itself to developing intuition for higher-order spectroscopic techniques.

ACKNOWLEDGMENTS

We acknowledge the support from the Natural Sciences and Engineering Research Council of Canada (NSERC) and the Ontario Trillium Scholarship.

DATA AVAILABILITY

The data that support the findings of this study are available from the corresponding author upon reasonable request. In addition, the code to generate all of the figures in this manuscript is available at GitHub.

REFERENCES

- W. M. Zhang, T. Meier, V. Chernyak, and S. Mukamel, *J. Chem. Phys.* **108**, 7763 (1998).
- T. Brixner, J. Stenger, H. M. Vaswani, M. Cho, R. E. Blankenship, and G. R. Fleming, *Nature* **434**, 625 (2005).
- M. Cho, H. M. Vaswani, T. Brixner, J. Stenger, and G. R. Fleming, *J. Phys. Chem. B* **109**, 10542 (2005).
- D. Abramavicius, B. Palmieri, D. V. Voronine, F. Šanda, and S. Mukamel, *Chem. Rev.* **109**, 2350 (2009).
- G. Panitchayangkoon, D. V. Voronine, D. Abramavicius, J. R. Caram, N. H. C. Lewis, S. Mukamel, and G. S. Engel, *Proc. Natl. Acad. Sci. U. S. A.* **108**, 20908 (2011).
- N. Christensson, H. F. Kauffmann, T. Pullerits, and T. Mančal, *J. Phys. Chem. B* **116**, 7449 (2012).
- J. H. Fetherolf and T. C. Berkelbach, *J. Chem. Phys.* **147**, 244109 (2017).
- S. J. Jang and B. Mennucci, *Rev. Mod. Phys.* **90**, 035003 (2018).
- C. D. Cruz, J. Yuan, C. Climent, N. T. Tierce, P. R. Christensen, E. L. Chronister, D. Casanova, M. O. Wolf, and C. J. Bardeen, *Chem. Sci.* **10**, 7561 (2019).
- A. J. Kiessling and J. A. Cina, *J. Chem. Phys.* **152**, 244311 (2020).
- P. Malý, S. Mueller, J. Lüttig, C. Lambert, and T. Brixner, *J. Chem. Phys.* **153**, 144204 (2020).
- J. Süß and V. Engel, *J. Chem. Phys.* **153**, 164310 (2020).
- S. Mukamel, *Principles of Nonlinear Optical Spectroscopy* (Oxford University Press, 1999).
- L. Yang, I. V. Schweigert, S. T. Cundiff, and S. Mukamel, *Phys. Rev. B* **75**, 125302 (2007).
- P. Huo and D. F. Coker, *J. Phys. Chem. Lett.* **2**, 825 (2011).
- A. Perdomo-Ortiz, J. R. Widom, G. A. Lott, A. Aspuru-Guzik, and A. H. Marcus, *J. Phys. Chem. B* **116**, 10757 (2012).
- J. Dostál, T. Mančal, R.-n. Augulis, F. Vácha, J. Pšenčík, and D. Zigmantas, *J. Am. Chem. Soc.* **134**, 11611 (2012).
- K. J. Karki, J. R. Widom, J. Seibt, I. Moody, M. C. Lonergan, T. Pullerits, and A. H. Marcus, *Nat. Commun.* **5**, 5869 (2014).
- J. Provazza, F. Segatta, M. Garavelli, and D. F. Coker, *J. Chem. Theory Comput.* **14**, 856 (2018).
- J. Dostál, F. Fennel, F. Koch, S. Herbst, F. Würthner, and T. Brixner, *Nat. Commun.* **9**, 2466 (2018).
- P. Malý and T. Mančal, *J. Phys. Chem. Lett.* **9**, 5654 (2018).
- S. M. Gallagher Faeder and D. M. Jonas, *J. Phys. Chem. A* **103**, 10489 (1999).
- N. Belabas and D. M. Jonas, *Opt. Lett.* **29**, 1811 (2004).
- M. K. Yezzbacher, N. Belabas, K. A. Kitney, and D. M. Jonas, *J. Chem. Phys.* **126**, 044511 (2007).
- P. F. Tekavec, J. A. Myers, K. L. M. Lewis, F. D. Fuller, and J. P. Ogilvie, *Opt. Express* **18**, 11015 (2010).
- J. Yuen-Zhou, J. J. Krich, and A. Aspuru-Guzik, *J. Chem. Phys.* **136**, 234501 (2012).
- V. Tiwari, W. K. Peters, and D. M. Jonas, *Proc. Natl. Acad. Sci. U. S. A.* **110**, 1203 (2013).
- H. Li, A. P. Spencer, A. Kortyna, G. Moody, D. M. Jonas, and S. T. Cundiff, *J. Phys. Chem. A* **117**, 6279 (2013).
- X. Leng, S. Yue, Y.-X. Weng, K. Song, and Q. Shi, *Chem. Phys. Lett.* **667**, 79 (2016).
- V. Perlík, J. Hauer, and F. Šanda, *J. Opt. Soc. Am. B* **34**, 430 (2017).
- C. L. Smallwood, T. M. Autry, and S. T. Cundiff, *J. Opt. Soc. Am. B* **34**, 419 (2017).
- T. N. Do, M. F. Gelin, and H.-S. Tan, *J. Chem. Phys.* **147**, 144103 (2017).
- D. Paleček, P. Edlund, E. Gustavsson, S. Westenhoff, and D. Zigmantas, *J. Chem. Phys.* **151**, 024201 (2019).
- A. Anda and J. H. Cole, "Two-dimensional spectroscopy beyond the perturbative limit: The influence of finite pulses and detection modes," *arXiv:2011.04343* (2020).

- ³⁵P. F. Tekavec, G. A. Lott, and A. H. Marcus, *J. Chem. Phys.* **127**, 214307 (2007).
- ³⁶M. Cho, *Two-Dimensional Optical Spectroscopy* (CRC Press, 2009).
- ³⁷M. Z. Peter Hamm, *Concepts and Methods of 2D Infrared Spectroscopy* (Cambridge University Press, 2011).
- ³⁸G. Nardin, T. M. Autry, K. L. Silverman, and S. T. Cundiff, *Opt. Express* **21**, 28617 (2013).
- ³⁹A. A. Bakulin, C. Silva, and E. Vella, *J. Phys. Chem. Lett.* **7**, 250 (2016).
- ⁴⁰V. Tiwari and D. M. Jonas, *J. Chem. Phys.* **148**, 084308 (2018).
- ⁴¹P. A. Rose and J. J. Krich, *J. Chem. Phys.* **150**, 214105 (2019).
- ⁴²P. A. Rose and J. J. Krich, "Efficient numerical method for predicting nonlinear optical spectroscopies of open systems," *J. Chem. Phys.* **154**, 034108 (2021); [arXiv:2008.05082](https://arxiv.org/abs/2008.05082).
- ⁴³V. Engel, *Comput. Phys. Commun.* **63**, 228 (1991).
- ⁴⁴M. Beck, A. Jackle, G. Worth, and H.-D. Meyer, *Phys. Rep.* **324**, 1 (2000).
- ⁴⁵K. Renziehausen, P. Marquetand, and V. Engel, *J. Phys. B: At., Mol. Opt. Phys.* **42**, 195402 (2009).
- ⁴⁶Y. Tanimura, *J. Chem. Phys.* **137**, 22A550 (2012).
- ⁴⁷J. R. Johansson, P. D. Nation, and F. Nori, *Comput. Phys. Commun.* **183**, 1760 (2012).
- ⁴⁸J. Yuen-Zhou, J. J. Krich, I. Kassal, A. S. Johnson, and A. Aspuru-Guzik, *Ultrafast Spectroscopy* (IOP Publishing, 2014).
- ⁴⁹J. Albert, M. Falge, M. Keß, J. G. Wehner, P.-P. Zhang, A. Eisfeld, and V. Engel, *J. Chem. Phys.* **142**, 212440 (2015).
- ⁵⁰Y.-a. Yan, *Chin. J. Chem. Phys.* **30**, 277 (2017).
- ⁵¹Y. Ke and Y. Zhao, *J. Chem. Phys.* **149**, 014104 (2018).
- ⁵²T. Mančal, Quantarhei: Molecular open quantum systems package (2020), <http://github.com/tmancal74/quantarhei>.
- ⁵³D. M. Jonas, *Annu. Rev. Phys. Chem.* **54**, 425 (2003).
- ⁵⁴T. N. Do, L. Chen, A. K. Belyaev, H.-S. Tan, and M. F. Gelin, *Chem. Phys.* **515**, 119 (2018).
- ⁵⁵J. Süß, J. Wehner, J. Dostál, T. Brixner, and V. Engel, *J. Chem. Phys.* **150**, 104304 (2019).
- ⁵⁶Z. Zhang, K. L. Wells, E. W. J. Hyland, and H.-S. Tan, *Chem. Phys. Lett.* **550**, 156–161 (2012).